JCTC Journal of Chemical Theory and Computation

pubs.acs.org/JCTC Article

Charge-Optimized Electrostatic Interaction Atom-Centered Neural Network Algorithm

Zichen Song, Jian Han, Graeme Henkelman, and Lei Li*

Cite This: J. Chem. Theory Comput. 2024, 20, 2088−2097 Read Online

ACCESS | Metrics & More | Article Recommendations | Supporting Information

ABSTRACT: Machine-learning algorithms have been proposed to capture electrostatic interactions by using effective partial charges. These algorithms often rely on a pretrained model for partial charge prediction using density functional theory-calculated partial charges as references, which introduces complexity to the force field model. The accuracy of the trained model also depends on the reliability of charge partition methods, which can be dependent on the specific system and methodology employed. In this study, we propose an atom-centered neural network (ANN) algorithm that eliminates the need for reference charges. Our algorithm requires only a single NN model for each element to obtain both atomic energy and charges. These atomic charges are then employed to compute electrostatic energies using the Ewald summation algorithm. Subsequently, the force field model is trained on total energy and forces, with the inclusion of electrostatic energy. To evaluate the performance of our algorithm, we conducted tests on three benchmark systems, including a Ge slab with an O adatom system, a TiO_2 crystalline system, and a Pd−O nanoparticle system. Our results demonstrate reasonably accurate predictions of partial charges and electrostatic interactions. This algorithm provides a self-consistent charge prediction strategy and possibilities for robust and reliable modeling of electrostatic interactions in machine-learning potentials.

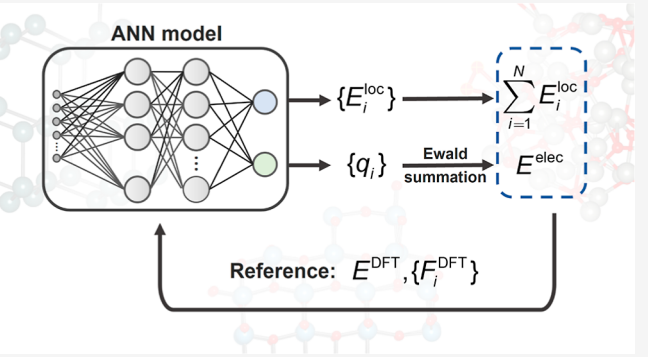

1. INTRODUCTION

Computer simulation approaches play a vital role in advancing our understanding of molecular systems in the fields of chemistry, biology, and materials science. The accuracy of the potential energy surface (PES) determines the reliability of the simulation results. Density functional theory (DFT) offers reasonable accuracy for constructing a PES, but its high computational cost limits the application to small system sizes and short time scales.[1] Empirical potentials based on a physical approximation are cost-effective alternatives for the PES description and have been widely used in molecular dynamics simulations of large systems. Nevertheless, empirical potentials can suffer from limited accuracy and transferability across various systems due to their parametrization for specific chemical environments.

In recent decades, machine learning techniques have emerged as powerful tools to "learn" the PES of atomic systems. Machine-learning potentials (MLPs) generated through these techniques, such as neural network potential (NNP),[2−10] Gaussian approximation potential,[11,12] graph convolutional networks potential,[13−15] etc., have demonstrated DFT-level accuracy with lower computational costs.[16−19] These MLPs have expanded the possibility for simulating larger systems and enable dynamic simulations on extended time scales with DFT accuracy. For example, MLPs have been used to study the phase behaviors of various materials, including Si,[20,21] Ga,[22] P,[23] bulk and two-dimensional H_2O systems,[24,25] etc. By utilizing MLPs, researchers have generated phase diagrams at DFT-level accuracy to uncover underlying mechanisms that were previously challenging to achieve using DFT.

Although these MLPs have achieved notable success, they typically focus on describing atomic interactions within a constrained atom-centered sphere defined by a radial cutoff. These algorithms do not compute charge information and often neglect long-range interactions. Behler classified these algorithms as second-generation machine-learning algorithms, in contrast to the first-generation algorithm developed by Doren and co-workers[26] which was applied to smaller systems. It is worth emphasizing that an accurate description of long-range interactions is crucial for capturing many material properties. Specifically, an accurate representation of partial charge information in MLPs is important because charge-transfer behavior at the molecular level plays a fundamental

Received: November 13, 2023
Revised: February 10, 2024
Accepted: February 12, 2024
Published: February 21, 2024

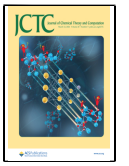

https://doi.org/10.1021/acs.jctc.3c01254
J. Chem. Theory Comput. 2024, 20, 2088−2097

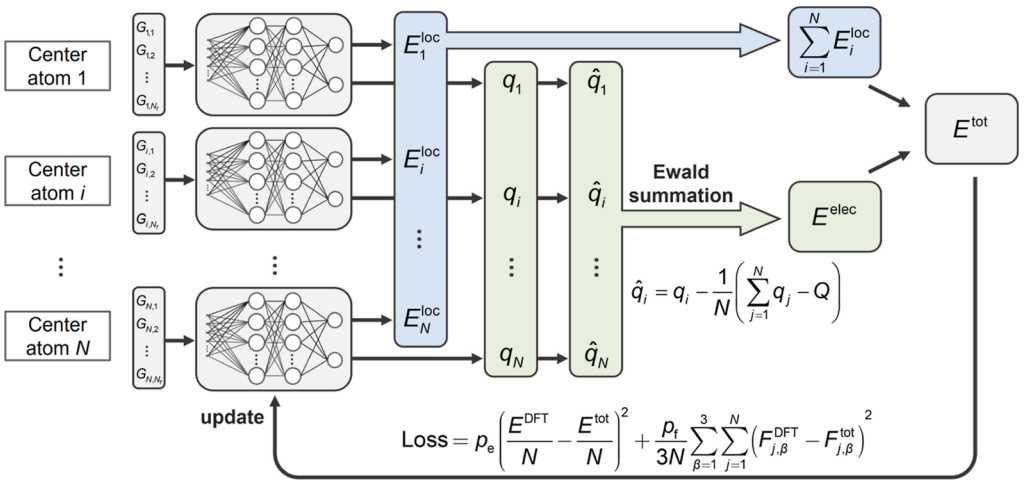

Figure 1. Flowchart of the charge-optimized electrostatic-interaction ANN algorithm. Two nodes are designed at the output layer of each NN model for the prediction of local atomic energies (E_i^{loc}) and charges (q_i), respectively. The charge value is then corrected to ensure charge conservation of the system. The corrected charge ($\hat{q}_i$) is used to calculate the electrostatic energy and forces with the Ewald summation method. $G_{i,n}$ represents the n-th ACSFs centered at the i-th atom. E_i^{loc}, E^{elec}, and E^{tot} represent the predicted local atomic energy of atom i, electrostatic energy of the structure, and total energy of the structure, respectively. Note that the form of the loss function is same with and without considering electrostatic interactions.

role in chemistry, physics, biology, and materials science.[27−30] For example, charge transfer occurs between adsorbate and electrodes in electrochemical reduction reaction,[31] ligands and metals in metal complexes,[32,33] as well as donors and acceptors in conjugated photovoltaic materials.[34,35] In these cases, long-range electrostatic interactions affect the properties, such as catalytic activity, solvation, and adsorption behavior. Therefore, adequately accounting for long-range interactions is essential for a comprehensive understanding and accurate prediction of these material properties.

Several algorithms have been developed to incorporate long-range electrostatic contributions into machine-learning models for total energy calculations. Deng et al.[36] presented electrostatic Spectral Neighbor Analysis Potential (eSNAP) for highly ionic α-Li_3N, where fixed charges were assigned to Li and N atoms to compute the electrostatic energy. This approach with constant charges is not applicable to material systems with charge redistribution behavior. Alternatively, Artrith et al.[37,38] proposed that a more versatile methodology utilizes two separate NN models. One NN model captures atomic partial charges as a function of local chemical environments, while the other NN model fits local atomic energies by subtracting the electrostatic energies from DFT total energies. This algorithm with environment-adaptive charges is known as a third-generation MLP. More recently, Behler, Goedecker, and their co-workers introduced fourth-generation high-dimensional NN potentials (4G-HDNNPs),[39,40] which employed charge equilibration (Qeq) algorithms to fit DFT charges. The atomic electronegativities were adjusted to ensure agreement between the charges obtained from the Qeq method and the DFT reference values, allowing the atomic charges to distribute optimally throughout the system. The adoption of the Qeq method demonstrated improved performance in incorporating charge effects into machine-learning models, enabling better representation of materials with varying charge distributions.[41,42] The effective atomic partial charges can also be indirectly trained through fitting the ab initio dipole moment, as implemented in PhysNet.[43] Additionally, the self-consistent field NN (SCFNN)[44] and deep potential long-range schemes[45] were developed to incorporate the electrostatic interaction using the Wannier center for the representation of electronic structure information. These models demonstrated effectiveness for organic molecules and liquid water systems.

These advancements have demonstrated success in incorporating electrostatic interactions in machine-learning models. However, they typically require an additional NN model for pretraining atomic partial charges or electrostatic energy, which adds complexity to the MLPs. Additionally, the use of ab initio partial charges (such as DFT charges) as target values for network training, as seen in 4G-HDNNPs, is subjective. DFT charges based on different charge partition schemes can yield varying numerical values, and their applicability depends on the specific system. There is a need to develop new machine-learning algorithms that are independent of the DFT reference charges.

In this work, we propose a charge-optimized atom-centered NN (ANN) algorithm that incorporates an electrostatic interaction. It allows the model to predict the atomic partial charges without relying on DFT partial charges. The algorithm simultaneously captures environment-dependent atomic partial charges and local atomic energy by using a single NN model. The capability of the scheme is benchmarked using three distinct material systems and chemical environments. The following section provides a detailed methodology of the algorithm, followed by the presentation of training results for representative material systems, including a Ge slab with O adatom, a TiO_2 crystalline system, and a Pd−O nanoparticle system.

2. COMPUTATIONAL DETAILS

2.1. Charge-Optimized Electrostatic Interaction ANN Algorithm. The partial charges of atoms are subject to the influence of their local chemical environments. The variation in their local chemical environments results in changes in atomic partial charges, thus impacting the total energy and atomic forces of the system. The NN models are potentially capable of learning and capturing these impacts by fitting the total energy and atomic forces without reference to DFT charges. To

https://doi.org/10.1021/acs.jctc.3c01254
J. Chem. Theory Comput. 2024, 20, 2088−2097

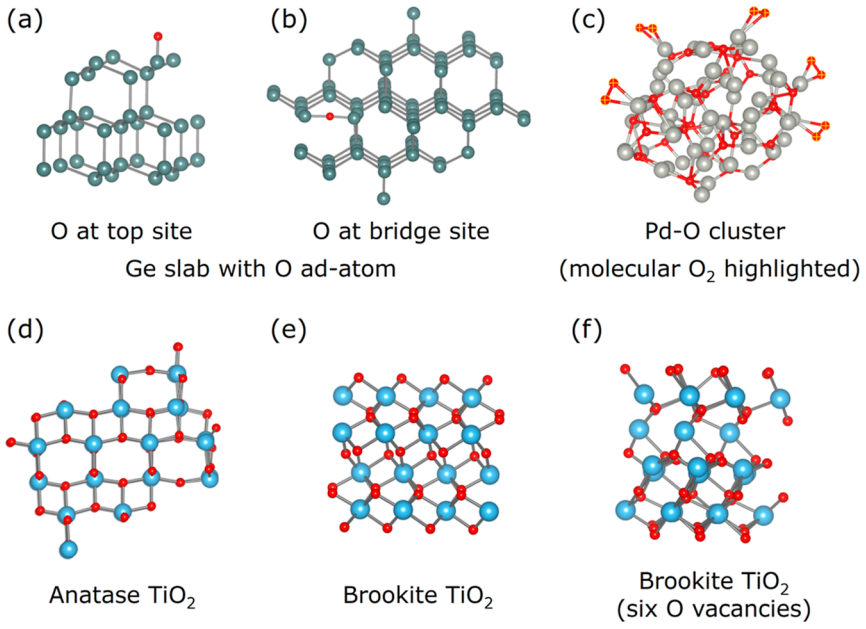

Figure 2. Atomic illustration of material systems used in this study. (a,b) Ge slab with O adatom system, (c) Pd−O nanoparticle system, where O atoms that are adsorbed on the nanoparticle surface are yellow, and (d−f) TiO_2 system, including the anatase and brookite crystalline structures, along with the brookite TiO_2 with six O vacancies. The atomic elements are color-coded as follows: Ge in green, Pd in gray, Ti in blue, and O in red.

achieve this, we extended the framework of the NN model proposed by Behler and Parrinello[37,38] (denoted as BPANN)[22] to incorporate electrostatic interactions with atomic partial charges as outputs of the NN model. This modification allows us to retain the original loss function while considering the influence of partial charges. The resulting algorithm, named the charge-optimized electrostatic-interaction ANN algorithm, is depicted in Figure 1 for a comprehensive overview.

As shown in Figure 1, we employed a NN model for each element with atomic local environments ($\mathbf{R}_i$) as inputs that are described by the modified atom-centered symmetry functions (ACSFs) $\mathbf{G}_i = \{G_{i,n}\}$, also known as descriptors (see the Supporting Information, Section S1 for details). $G_{i,n}$ represents the n-th ACSF centered at the i-th atom. Different from BPANN, we utilized two output nodes that are, respectively, responsible for the local atomic energy E_i^{loc}, excluding electrostatic interaction, and partial charges q_i of atom i. Upon NN mapping, they are expressed as a function of the descriptors $\mathbf{G}_i$ in the form of $q_i(\mathbf{G}_i(\mathbf{R}_i))$ and $E_i^{\mathrm{loc}}(\mathbf{G}_i(\mathbf{R}_i))$. In order to guarantee charge conservation in the system, a charge correction method[43] is applied. The final predicted charge $\hat{q}_i(\mathbf{G}(\mathbf{R}))$ is given by eq 1. Note that the charge obtained from the ANN algorithm described in the following sections is the final predicted charge.

$$\hat{q}_i = q_i - \frac{1}{N}\left(\sum_{j=1}^{N} q_j - Q\right) \tag{1}$$

where N and Q are the total number of atoms and the total charge of the system, respectively. The charge correction method eliminates any net charge in the system (Table S1). The predicted charge $\hat{q}_i$ was then used in the Ewald summation method to compute the electrostatic energy E^{elec} of the system. For the charge-neutralized system, Ewald summation consists of three terms:[46] the real space sum $E^{(\mathrm{r})}$, the reciprocal sum $E^{(\mathrm{k})}$, and the self-term $E^{(\mathrm{s})}$. For the simplicity of this paper, the specific expressions of these three terms are shown in the Supporting Information (Section S2). Hereby, we have the form of electrostatic energy, as shown in eq 2.

$$\begin{aligned} E^{\mathrm{elec}}(\mathbf{R}, \mathbf{q}) = {} & E^{(\mathrm{r})}(\mathbf{R}_{ij}, \hat{q}_i(\mathbf{G}(\mathbf{R})), \hat{q}_j(\mathbf{G}(\mathbf{R}))) \\ & + E^{(\mathrm{k})}(\mathbf{R}_i, \hat{q}_i(\mathbf{G}(\mathbf{R}))) \\ & + E^{(\mathrm{s})}(\hat{q}_i(\mathbf{G}(\mathbf{R}))). \end{aligned} \tag{2}$$

Then, the total energy was calculated as the sum of the local atomic energy and electrostatic energy with eq 3.

$$E^{\mathrm{tot}}(\mathbf{R}, \mathbf{q}) = \sum_{i}^{N} E_i^{\mathrm{loc}}(\mathbf{R}_i) + E^{\mathrm{elec}}(\mathbf{R}, \mathbf{q}) \tag{3}$$

We calculated atomic forces using the mathematical expression of the energy shown in eq 3. From the chain rule, the local atomic forces $F_{i,\beta}^{\mathrm{loc}}$ on atom i in the direction β can be expressed as eq 4.

$$F_{i,\beta}^{\mathrm{loc}} = -\sum_{i=1}^{N} \frac{\partial E_i^{\mathrm{loc}}}{\partial \beta_i} = -\sum_{i=1}^{N}\sum_{m=1}^{M_i} \frac{\partial E_i^{\mathrm{loc}}}{\partial G_{i,m}} \frac{\partial G_{i,m}}{\partial \beta_i} \tag{4}$$

where β_i is the distance vector component in the direction β and M_i is the number of ACSFs. The electrostatic forces $F_{i,\beta}^{\mathrm{elec}}$ on atom i in the direction β can be derived by differentiating electrostatic energy E^{elec} from Ewald summation with respect to β_i.

$$F_{i,\beta}^{\mathrm{elec}} = -\frac{\partial E^{\mathrm{elec}}}{\partial \beta_i} = -\frac{\partial E^{(\mathrm{r})}}{\partial \beta_i} - \frac{\partial E^{(\mathrm{k})}}{\partial \beta_i} - \frac{\partial E^{(\mathrm{s})}}{\partial \beta_i} \tag{5}$$

Note that the derivatives of the predicted charges are included, since they are a function of the local chemical environments in our ANN algorithm. The specific form of the electrostatic

https://doi.org/10.1021/acs.jctc.3c01254
J. Chem. Theory Comput. 2024, 20, 2088−2097

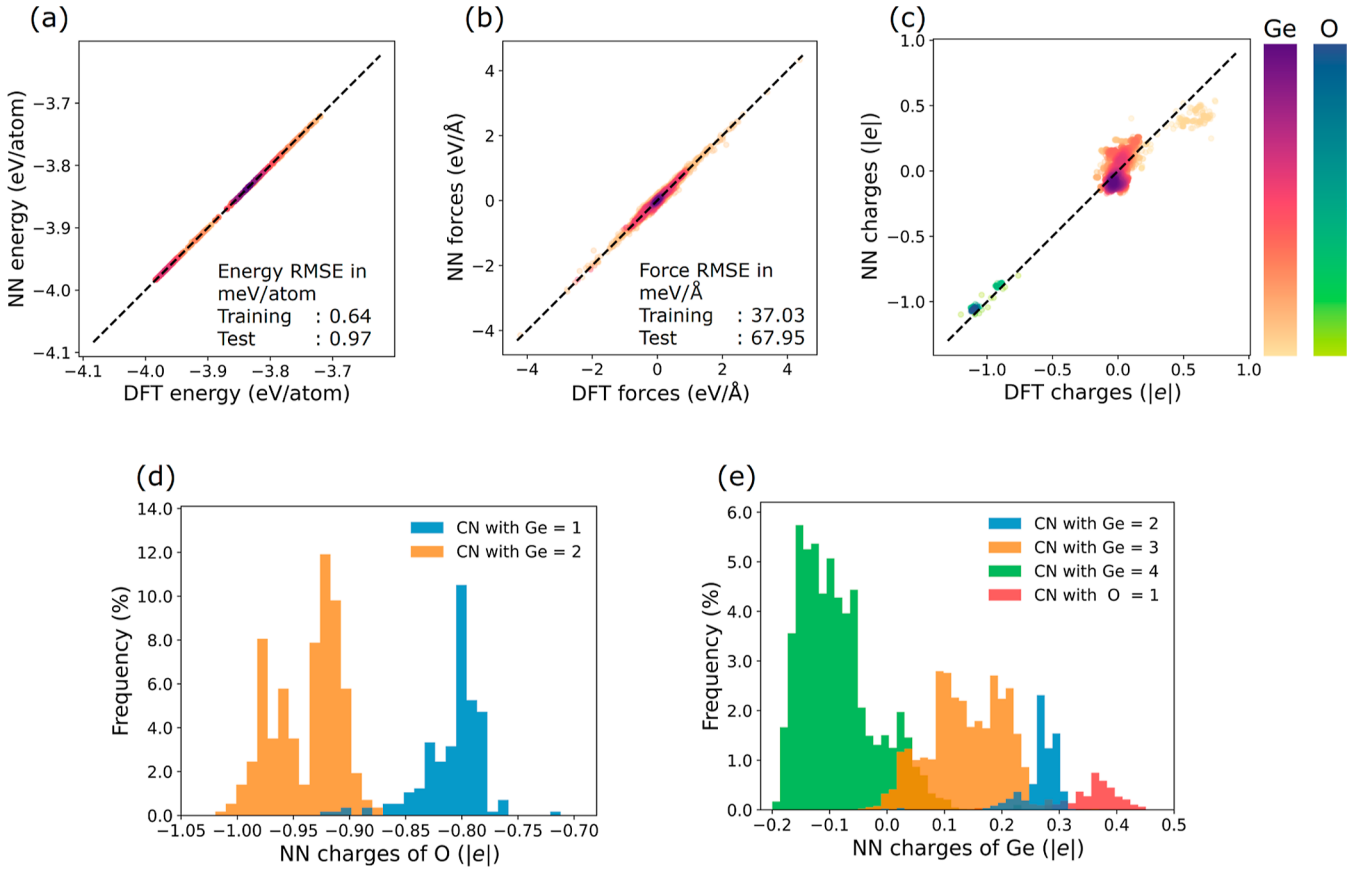

Figure 3. Scatter plots illustrating correlations of (a) energies, (b) forces, and (c) charges calculated by the ANN algorithm with corresponding DFT values for the Ge slab with O adatom system. Histograms of charge distribution of (d) O and (e) Ge atoms with different local environments. (d) Orange and blue histograms represent the charge distribution of O atoms coordinated with 1 and 2 Ge atoms, respectively; (e) blue, orange, green, and red histograms show the charge distribution of Ge atoms coordinated with 2, 3, and 4 Ge atoms, as well as 1 O atom, respectively.

forces and additional details can be found in Section S2 of the Supporting Information.

The total energy and atomic forces were trained to reference values by minimizing the loss function defined in eq 6. The loss function shares the same form as that of the traditional ANN algorithm.

$$\text{loss} = p_e\left(\frac{E^{\text{DFT}}}{N} - \frac{E^{\text{tot}}}{N}\right)^2 + \frac{p_f}{3N}\sum_{\beta=1}^{3}\sum_{j=1}^{N}(F_{j,\beta}^{\text{DFT}} - F_{j,\beta}^{\text{tot}})^2 \quad (6)$$

where p_e and p_f are the energy and force coefficient, respectively. Unlike previously reported algorithms that involve two-step training processes,[37−39] our algorithm trains the local atomic energies and partial charges simultaneously by varying the weight and bias of the NN model. The ratio of the electrostatic term and the local atomic term is determined by the NN model, allowing the charge partitioning process to be completed based on minimizing the loss function without relying on predefined values. Our training scheme is based on self-consistent charge partitioning, which is the key motivation behind this paper.

2.2. Development of Machine-Learning Potentials. We implemented our charge-optimized electrostatic-interaction ANN algorithm in the python atom-centered machine-learning force field (PyAMFF) package.[47] Throughout this study, we employed NN architectures with two hidden layers consisting of 108 and 32 neurons. The tanh function was selected as the activation function for these models. To optimize the NN models, we adopted the loss function in eq 6 with p_e = 1.0 eV^{-1} and p_f = 0.1 $Å^2 \cdot eV^{-1}$. The weights connecting each layer were initialized from a normal distribution and then optimized to minimize the loss function with the Limited-Broyden-Fletcher-Goldfarb-Shanno (L-BFGS) algorithm. For data set preparation, we randomly divided the structures, allocating 10% as the test set and 90% as the training set. Specific hyperparameters of ACSFs for each system are detailed in Tables S3−S8. Eight independent NN models were trained for each system, and the one exhibiting the best performance is reported here.

2.3. Data Set Preparation and DFT Calculations. To validate the reliability of our algorithm, we prepared data sets of three binary material systems with diverse structures: a Ge slab with an O adatom system, a TiO_2 crystalline system, and a Pd−O nanoparticle system. Note that our focus is not on developing general MLP models for these systems, and the completeness of the training data set is not considered here. For the data set of the Ge slab with an O adatom, we obtained 736 structures from an open-source data set repository: Open Catalyst 2020 (OC20).[48] The data set includes local minimum and nonequilibrium structures obtained from the optimization of randomly sampled low-Miller-index facets of Ge (examples are shown in Figure 2e). The TiO_2 crystalline system data set contains stoichiometric anatase and brookite crystal structures (Figure 2a,b), with 650 and 913 structures, respectively. To account for nonstoichiometric situations, we also included 883

https://doi.org/10.1021/acs.jctc.3c01254
J. Chem. Theory Comput. 2024, 20, 2088−2097

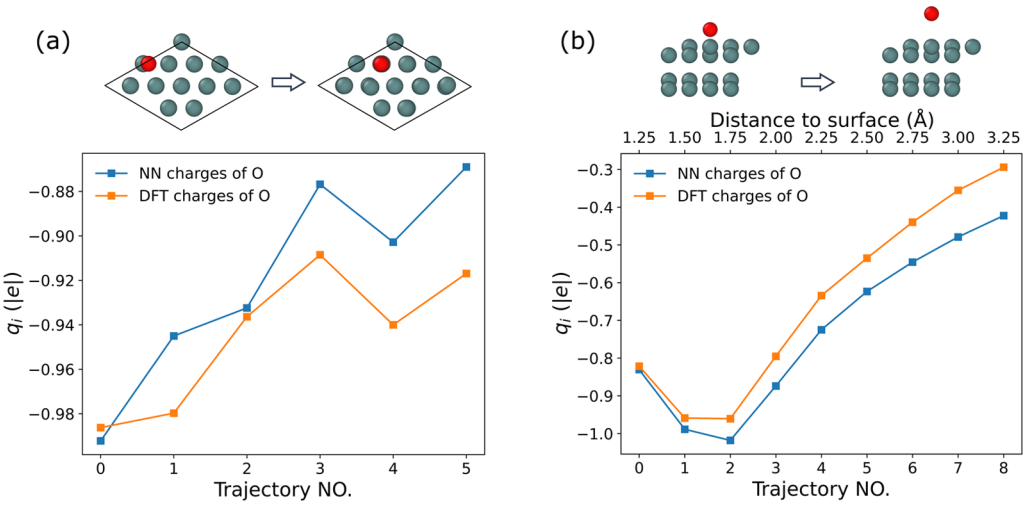

Figure 4. Charge variation of the O atom when (a) shifting from the 3-fold hollow site to the top site and (b) displaced from the Ge slab. The green and red spheres represent Ge and O atoms, respectively. The orange lines show the charges of each structure calculated by DFT. The blue lines show the NN-predicted charges of each structure computed from the same NN model used in Figure 3.

brookite TiO_2 structures with six O vacancies (Figure 2c). Overall, a total of 2446 structures were included in the TiO_2 crystalline system data set. The Pd−O data set contains 1293 structures of Pd−O amorphous nanoparticles. These nanoparticles have a diverse number of absorbed O_2 molecules on their surfaces. Specifically, the O atoms can be found either in coordination with Pd atoms within the nanoparticles (referred to as embedded O) or as absorbed molecular O_2 on the nanoparticle surface (as highlighted in Figure 2d). The nanoparticle sizes vary, ranging from 32 atoms to 97 atoms. A vacuum space of 10 to 15 Å was maintained to avoid interactions between neighboring images.

The reference energies and forces for the TiO_2 crystalline and Pd−O nanoparticle systems were calculated by DFT as implemented in the VASP package.[49] The project-augmented wave method and plane wave basis sets with an energy cutoff at 500 eV were applied to represent the core−valence electron interaction. The exchange−correlation interaction was treated within the generalized gradient approximation by using the Perdew−Burke−Ernzerhof functional. *K*-point meshes with a maximum spacing of 0.05 $Å^{-1}$ were employed for all DFT calculations.

3. RESULTS AND DISCUSSION

3.1. Ge Slab with O Adatom System. We first tested our algorithm on a simple system involving a Ge slab (111) surface with one O adatom. The training scheme illustrated in Figure 1 was employed to incorporate electrostatic interaction, and no DFT charge information was provided during the training process. The energy and forces obtained from the NN model against the DFT method are presented in Figure 3a,b, showing a tight distribution along the $y = x$ line for both energy and forces, giving root mean square errors (RMSEs) of 0.64 meV/atom and 37.03 meV/Å for the training set, respectively. Comparable RMSEs are obtained for the test set with values of 0.97 meV/atom and 67.95 meV/Å, respectively. Note that we did not observe an improvement in the performance for energy and force evaluation over the traditional ANN algorithm, similar to previous reports.[50] Instead, we surprisingly found that our new algorithm generates reasonably accurate predictions on atomic charges, although there is no incorporation of DFT charge information during the training.

Figure 3c shows the correlation between the NN-predicted and DFT Bader charges for the test set, with the corresponding zoomed-in figures for the O and Ge atoms shown in Figure S7. The local environment analysis of the O and Ge atoms was conducted by calculating the corresponding coordination number (CN) and the results are presented in Figure 3d,e, respectively. As illustrated in Figure 3c, the predicted charges from the ANN method align along the $y = x$ line when compared to the DFT charges, generating RMSE values of 0.05 and 0.10 |*e*| for O and Ge (Table S2), respectively. This alignment underscores the accuracy of our NN model in predicting atomic charges. Notably, O atoms with CN = 1 and 2 (corresponding to the O atom on the hollow and top sites) manifest charges with mean values of −0.8 and −0.95 |*e*|, respectively. The distribution of these charges closely follows the $y = x$ line, indicating robust agreement between predicted charges and DFT values. For Ge atoms, the accuracy of the predicted charges relies on their coordination environment. A substantial portion of Ge atoms in the data set are surrounded by 3 or 4 Ge atoms and do not directly interact with the O atom. For these Ge atoms, no obvious charge transfer is observed. The ANN algorithm captures this information, resulting in predicted charges near 0.0 |*e*|. Nevertheless, a small portion of Ge atoms that form bonds with the O atom have mean predicted charges of 0.4 |*e*|, which is lower than the DFT charges (Figure S7b). This discrepancy potentially stems from an insufficiency in local environments available for this specific category of Ge atoms.

To further validate the accuracy of the ANN method in predicting charges, we selected two displacements of the O atom on the Ge slab. The first involved shifting the O atom from one 3-fold hollow site to a top site, while the second moved the oxygen atoms away from the slab. Along these directions, we monitored the O charge using the developed NN models and the DFT-based Bader charge analysis method.[51] Figure 4a,b shows the charge variation of the O atom obtained from the NN model and the Bader charge analysis and shows that our method captures the trend in variation of the O charges in comparison to the results

https://doi.org/10.1021/acs.jctc.3c01254
J. Chem. Theory Comput. 2024, 20, 2088−2097

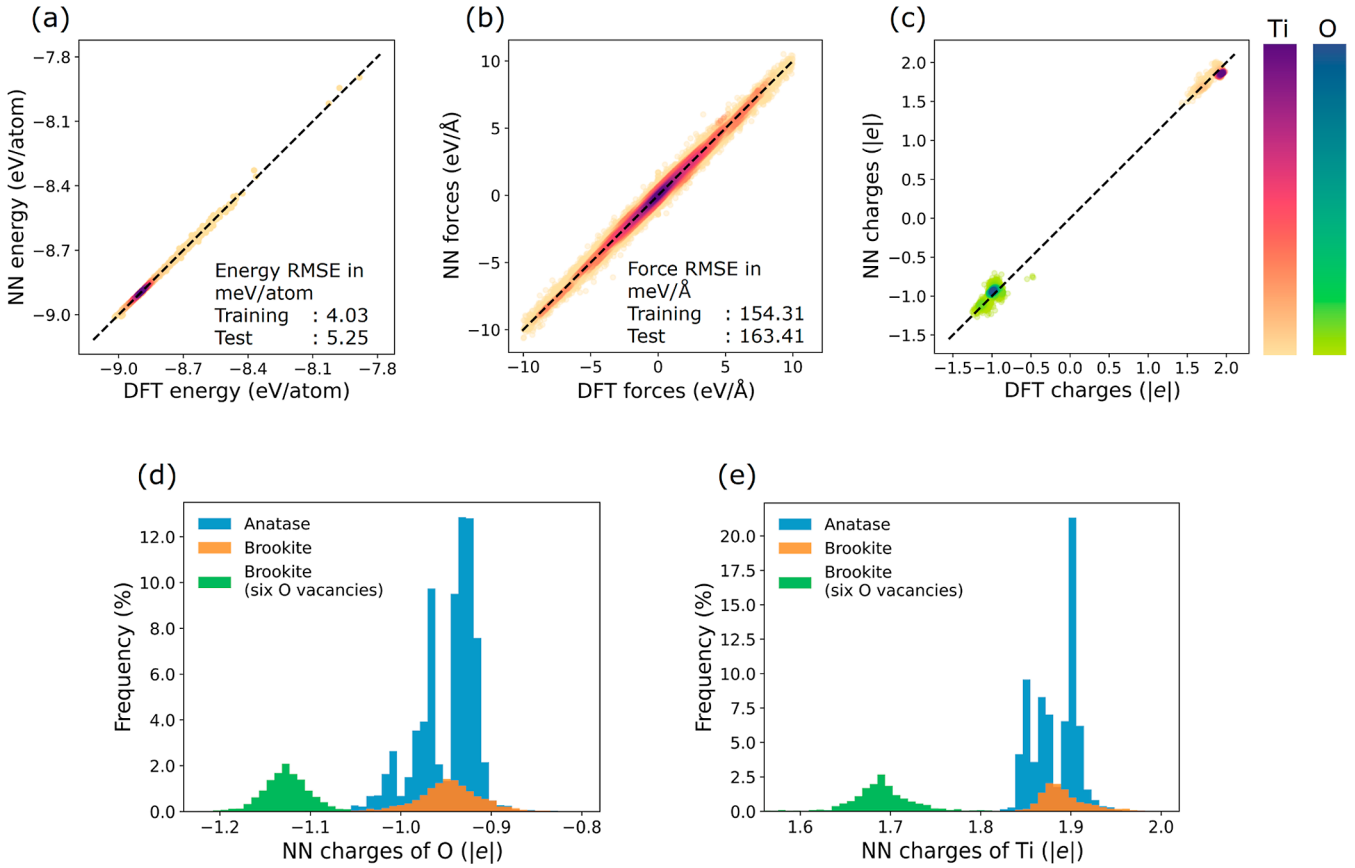

Figure 5. Scatter plots illustrating the correlation of (a) energies, (b) forces, and (c) charges calculated by the ANN algorithm with the corresponding DFT values for the TiO_2 crystalline system. Histograms of charge distribution of (d) O and (e) Ti atoms with different local environments. Blue, orange, and green histograms represent the charge distribution of O and Ti in anatase, perfect, and O-vacancy-defected brookite TiO_2, respectively.

obtained from the DFT method. In the first direction (Figure 4a), the O adatom undergoes a transition from the 3-fold hollow site to a top site, resulting in a subtle increment in the charge of the adatom as per DFT findings. This effect arises due to the diminished interaction between O and Ge during the shifting processes. Notably, our NN model accurately predicts this trend, aligning well with DFT. In the second direction, the O atom is moved away from the Ge slab, altering the Ge−O distance from 1.25 to 3.25 Å. According to the DFT results, the O charge experiences a decrease as the Ge−O distance changes from 1.25 to the equilibrium distance of 1.73 Å (Figure 4b). Beyond this equilibrium point, further extension of the Ge−O distance leads to an increase in the O charges, indicating reduced electron transfer from Ge to O. Remarkably, our NN models capture and follow this trend of charge variation for the O atom as the Ge−O distance changes. This observation demonstrates that our charge-optimized ANN scheme has the capability to effectively learn atomic charges by incorporating electrostatic interactions.

In summary, the developed ANN algorithm learns atomic charges as a function of the local atomic environment. The model's capability is evident in its ability to accurately predict charges for various atomic configurations, with notable successes in capturing the charge distribution for O atoms with distinct CNs and discerning the intricacies of charge transfer for Ge atoms engaged in direct interactions with O atoms.

3.2. TiO_2 Crystalline System. The second material system studied contains TiO_2 crystalline structures consisting of relaxation trajectories for three distinct structures: anatase, brookite, and brookite with six O vacancies (denoted as vac-brookite TiO_2) structures. The stoichiometric balance inherent in the crystalline framework helps equilibrate the distribution of local environments for both Ti and O atoms. Figure 5a,b shows the predicted energies and forces from the NN model against the reference DFT values. The tight distribution observed in both figures shows good agreement between the NN-predicted values and the DFT data. The performance of the NN model remains consistent across both the training and test sets, yielding energy RMSEs of 4.03 and 5.25 meV/atom and force RMSEs of 154.31 and 163.41 meV/Å, respectively. These data show that our algorithm effectively captures the energy and force within each distinct local environment present in the TiO_2 data set.

In the energy and force evaluation, our NN model performed concurrent calculations of charges associated with individual Ti and O atoms, as shown in Figure 1. These charges are presented in Figure 5c, showing the predicted charges relative to the DFT for the test set. Predicted charges for the O atoms exhibit a range spanning from −1.2 to −0.75 |*e*|, while Ti atoms are positively charged with values from 1.2 to 2.0 |*e*|. Zoomed-in figures for Ti and the O atoms are provided in Figure S8. These predicted charge values are aligned with the atomic charges obtained from the reference DFT values with RMSE values of 0.07 and 0.06 |*e*| for Ti and O (Table S2),

https://doi.org/10.1021/acs.jctc.3c01254
J. Chem. Theory Comput. 2024, 20, 2088−2097

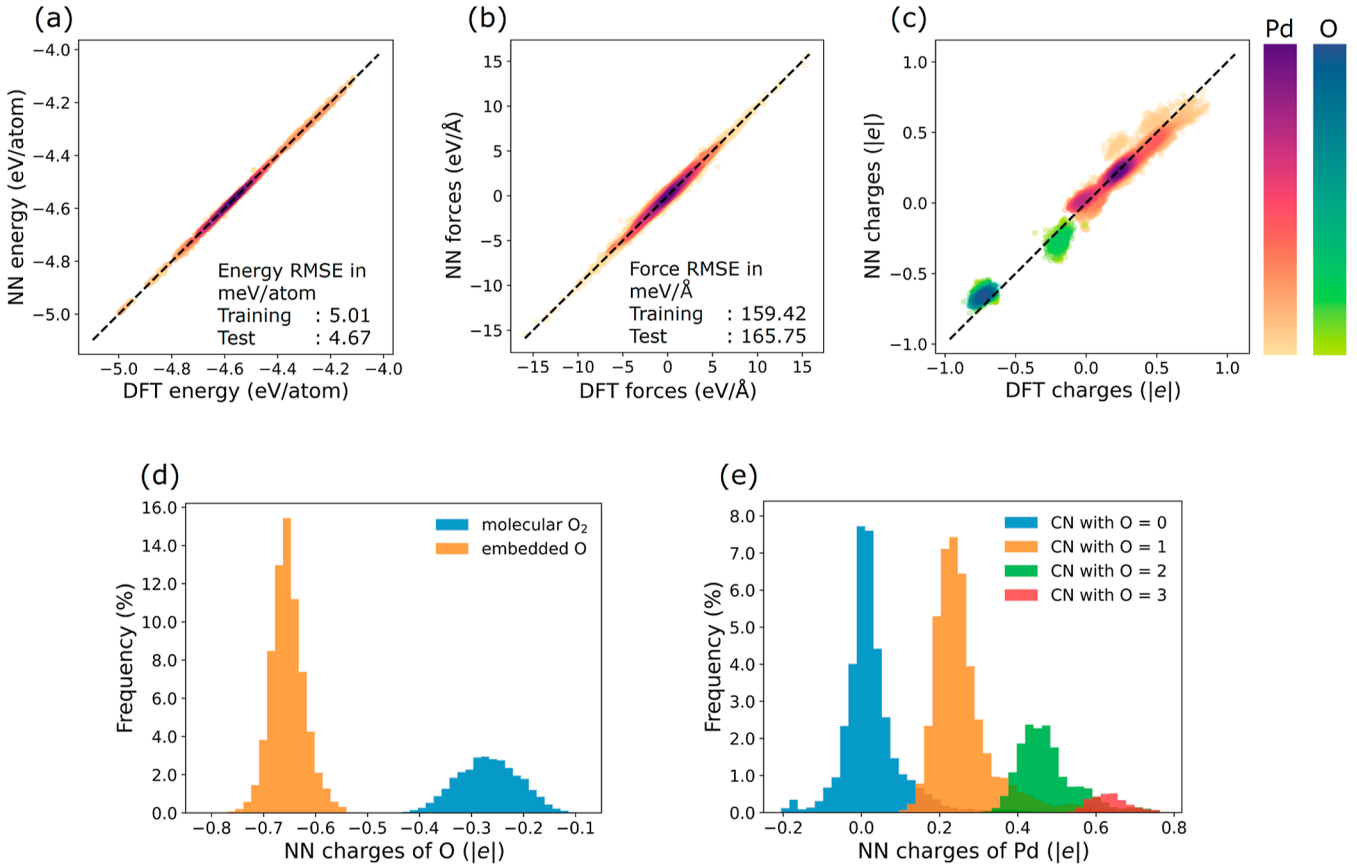

Figure 6. Scatter plots illustrating the correlation of (a) energies, (b) forces, and (c) charges calculated by the ANN algorithm with the corresponding DFT values for the Pd−O nanoparticle system. Histograms of charge distribution of (d) O and (e) Pd with different local environments. (d) Orange and blue histograms represent the charge distribution of embedded O and molecular O_2; (e) blue, orange, green, and red histograms represent the charge distribution of Ti atoms with CN from 0 to 3, respectively.

respectively, thereby demonstrating the efficacy of our ANN algorithm for charge prediction.

To explore the local-environment dependence of atomic charges, we plotted the charge distributions of O and Ti atoms across all structures in the data set based on three different crystal structures (Figure 6). As shown in Figure 5d,e, our NN model effectively distinguishes between O and Ti atoms in anatase and those in brookite TiO_2. In the case of perfect anatase, the mean charges on the O and Ti atoms are −0.95 and 1.90 |e|, respectively, whereas the corresponding values for perfect brookite TiO_2 are −0.94 and 1.88 |e|. This observed difference in charges implies a more pronounced charge transfer occurring in anatase TiO_2, in line with the DFT results. Remarkably, the NN model successfully predicted changes in oxidation states when an oxygen vacancy is induced in brookite TiO_2. As shown in Figure 5d,e, apparent shifts in charge distributions of the O and Ti atoms are observed in the vac-brookite TiO_2 despite both exhibiting distribution patterns akin to those in the perfect system. The peak positions shift from −0.94 to −1.13 for O and from 1.88 to 1.69 |e| for Ti. This shift indicates a reduction in the oxidation state of Ti due to the removal of O atoms from the lattice. Simultaneously, each remaining O atom in the lattice gains charge to maintain overall system neutrality.

3.3. Pd−O Nanoparticle System. Finally, we evaluated our methods using a Pd−O nanoparticle system characterized by amorphous structures. The training data set encompassed oxidized Pd nanoparticles, as well as nanoparticles with adsorbed oxygen atoms or molecules, thus providing a diverse array of chemical environments for Pd. Figure 6a,b shows the correlation of energy and forces predicted by the NN model and the DFT values. The energy RMSE for the Pd−O nanoparticle training and testing sets are 5.01 and 4.67 meV/atom, respectively. The force RMSEs are 159.42 and 165.75 meV/Å, respectively.

Figure 6c presents a comparison of atomic charges obtained from our ANN algorithm and the reference DFT method for the test set. For a more detailed examination of this correlation, refer to the enlarged figures in Figure S9. Our NN model managed to predict atomic charges for both Pd and O atoms with RMSE values of 0.07 and 0.09 |e|, respectively, in close agreement with those from DFT. Looking into the details of the coordination environment, shown in Figure 6d,e, Pd atoms in the nanoparticles exhibit more diverse coordination environments with O as compared to Ge atoms in the Ge slab system and the Ti atoms in the crystalline TiO_2 systems. This diversity leads to a wider distribution of charges from −0.25 to 1.0 |e| (Figure 6c). Specifically, Pd atoms can be classified into four types based on their interaction with O, resulting in Pd atoms binding with 0, 1, 2, and 3 O atoms. Our NN model successfully captured these distinct patterns, generating charge distributions peaking at 0.05, 0.25, 0.45, and 0.67 |e| (Figure 6e), respectively. These findings correlate well with the DFT results, effectively reflecting the changes in the oxidation state of Pd due to varying O atom bindings. For O atoms, two distinct charge distribution patterns are observed, peaking at

https://doi.org/10.1021/acs.jctc.3c01254
J. Chem. Theory Comput. 2024, 20, 2088−2097

−0.65 and −0.30 |e|, corresponding to atomic and molecular oxygen, respectively.

4. CONCLUSIONS

In conclusion, we introduced an ANN algorithm that explicitly integrates long-range electrostatic interactions. This algorithm generates environment-dependent charges and atomic energies within a single NN model. The former describes electrostatic interactions, while the latter represents local atomic interactions. This strategy empowers the NN model with the capability to predict atomic charges, relying solely on DFT energies and forces as references, thus eliminating the need for reference charge data. The efficacy of this algorithm is evaluated through three benchmark systems: a Ge slab with an O adatom system, a crystalline TiO_2 system, and a Pd−O nanoparticle system. The computed atomic partial charges exhibit a remarkable correlation with the DFT charges derived through Bader charge analysis. This correlation underscores the NN models' capacity to fit the electrostatic interactions independently of DFT charges.

The algorithm we developed here has demonstrated reasonable accuracy in predicting atomic charges, suggesting advancements in the development of self-consistent methods for the calculation of atomic charges within MLPs. Nonetheless, the inclusion of a long-range electrostatic interaction did not yield anticipated improvements in energy and force evaluation. A deeper exploration of how hyperparameters influence the performance of the ANN algorithm is crucial for refining its effectiveness. Further improvement in the charge prediction accuracy is also needed, especially in regions where there is limited variation in atomic charges. Additionally, the potential applicability of this algorithm to non-neutral systems has yet to be investigated. Introducing the Qeq scheme is potentially necessary to improve the accuracy of atomic charge prediction and make it suitable for non-neutral systems. Computational efficiency is another barrier preventing the actual implementation of the ANN algorithm described here. The implementation of the Ewald summation scheme results in a slowdown of both the training and energy and force evaluation processes. To overcome these barriers, further optimization is required for the entire ANN algorithm as well as the Ewald summation scheme. This optimization is essential to broaden the application of the charge-optimized ANN algorithm.

■ ASSOCIATED CONTENT

Data Availability Statement

The data that support the findings of this study are available from the corresponding author upon reasonable request.

Supporting Information

The Supporting Information is available free of charge at https://pubs.acs.org/doi/10.1021/acs.jctc.3c01254.

Specific expressions of Ewald summation used in this paper; forms of electrostatic forces and detailed implementation; charge distributions of ANN prediction and DFT calculation from the test set of three systems; zoomed figures emphasizing charges calculated by the ANN algorithm for each element of three systems; residual charge from training scheme without charge correction method; and hyper-parameters of ACSFs depending on specific system and element type (PDF)

■ AUTHOR INFORMATION

Corresponding Author

Lei Li − *Shenzhen Key Laboratory of Micro/Nano-Porous Functional Materials (SKLPM), Department of Materials Science and Engineering, Southern University of Science and Technology, Shenzhen 518055, China;* orcid.org/0000-0003-2882-2447; Email: lil33@sustech.edu.cn

Authors

Zichen Song − *Shenzhen Key Laboratory of Micro/Nano-Porous Functional Materials (SKLPM), Department of Materials Science and Engineering, Southern University of Science and Technology, Shenzhen 518055, China; Department of Materials Science and Engineering, City University of Hong Kong, Hong Kong, China;* orcid.org/0000-0002-7592-4481

Jian Han − *Department of Materials Science and Engineering, City University of Hong Kong, Hong Kong, China;* orcid.org/0000-0002-3800-9436

Graeme Henkelman − *Department of Chemistry, the University of Texas at Austin, Austin, Texas 78712, United States; Institute for Computational Engineering and Sciences, the University of Texas at Austin, Austin, Texas 78712, United States;* orcid.org/0000-0002-0336-7153

Complete contact information is available at: https://pubs.acs.org/10.1021/acs.jctc.3c01254

Notes

The authors declare no competing financial interest.

■ ACKNOWLEDGMENTS

This work was supported by Training Program of the Major Research Plan of the National Natural Science Foundation of China (no. 92270103), Shenzhen fundamental research funding (JCYJ20210324115809026), and Shenzhen Key Laboratory of Micro/Nano-Porous Functional Materials (SKLPM) (ZDSYS20210709112802010). The theoretical calculations were supported by Center for Computational Science and Engineering of Southern University of Science and Technology. The work at UT Austin was supported by NSF CHE-2102317, the Welch Foundation (F-1841), and the Texas Advanced Computing Center.

■ REFERENCES

(1) Car, R.; Parrinello, M. Unified Approach for Molecular Dynamics and Density-Functional Theory. *Phys. Rev. Lett.* **1985**, *55*, 2471−2474.

(2) Behler, J.; Parrinello, M. Generalized Neural-Network Representation of High-Dimensional Potential-Energy Surfaces. *Phys. Rev. Lett.* **2007**, *98*, 146401.

(3) Behler, J. Atom-Centered Symmetry Functions for Constructing High-Dimensional Neural Network Potentials. *J. Chem. Phys.* **2011**, *134*, 074106.

(4) Artrith, N.; Urban, A. An Implementation of Artificial Neural-Network Potentials for Atomistic Materials Simulations: Performance for TiO2. *Comput. Mater. Sci.* **2016**, *114*, 135−150.

(5) Khorshidi, A.; Peterson, A. A. Amp: A Modular Approach to Machine Learning in Atomistic Simulations. *Comput. Phys. Commun.* **2016**, *207*, 310−324.

(6) Schütt, K. T.; Sauceda, H. E.; Kindermans, P.-J.; Tkatchenko, A.; Müller, K. R. SchNet - A Deep Learning Architecture for Molecules and Materials. *J. Chem. Phys.* **2018**, *148*, 241722.

(7) Yao, K.; Herr, J. E.; Toth, D. W.; Mckintyre, R.; Parkhill, J. The TensorMol-0.1 Model Chemistry: A Neural Network Augmented with Long-Range Physics. *Chem. Sci.* **2018**, *9*, 2261−2269.
(8) Nebgen, B.; Lubbers, N.; Smith, J. S.; Sifain, A. E.; Lokhov, A.; Isayev, O.; Roitberg, A. E.; Barros, K.; Tretiak, S. Transferable Dynamic Molecular Charge Assignment Using Deep Neural Networks. *J. Chem. Theory Comput.* **2018**, *14*, 4687−4698.
(9) Singraber, A.; Behler, J.; Dellago, C. Library-Based LAMMPS Implementation of High-Dimensional Neural Network Potentials. *J. Chem. Theory Comput.* **2019**, *15*, 1827−1840.
(10) Zhang, Y.; Xia, J.; Jiang, B. Physically Motivated Recursively Embedded Atom Neural Networks: Incorporating Local Completeness and Nonlocality. *Phys. Rev. Lett.* **2021**, *127*, 156002.
(11) Bartók, A. P.; Csányi, G. Gaussian Approximation Potentials: A Brief Tutorial Introduction. *Int. J. Quantum Chem.* **2015**, *115*, 1051−1057.
(12) Bartók, A. P.; Payne, M. C.; Kondor, R.; Csányi, G. Gaussian Approximation Potentials: The Accuracy of Quantum Mechanics, without the Electrons. *Phys. Rev. Lett.* **2010**, *104*, 136403.
(13) Kearnes, S.; McCloskey, K.; Berndl, M.; Pande, V.; Riley, P. Molecular Graph Convolutions: Moving beyond Fingerprints. *J. Comput. Aided Mol. Des.* **2016**, *30*, 595−608.
(14) Xie, T.; Grossman, J. C. Crystal Graph Convolutional Neural Networks for an Accurate and Interpretable Prediction of Material Properties. *Phys. Rev. Lett.* **2018**, *120*, 145301.
(15) Wang, Y.; Fass, J.; Stern, C. D.; Luo, K.; Chodera, J. Graph Nets for Partial Charge Prediction. *arXiv* **2019**, arXiv:1909.07903.
(16) Behler, J. Perspective: Machine Learning Potentials for Atomistic Simulations. *J. Chem. Phys.* **2016**, *145*, 170901.
(17) Botu, V.; Batra, R.; Chapman, J.; Ramprasad, R. Machine Learning Force Fields: Construction, Validation, and Outlook. *J. Phys. Chem. C* **2017**, *121*, 511−522.
(18) Brockherde, F.; Vogt, L.; Li, L.; Tuckerman, M. E.; Burke, K.; Müller, K. R. Bypassing the Kohn-Sham Equations with Machine Learning. *Nat. Commun.* **2017**, *8*, 872.
(19) Noé, F.; Tkatchenko, A.; Müller, K. R.; Clementi, C. Machine Learning for Molecular Simulation. *Annu. Rev. Phys. Chem.* **2020**, *71*, 361−390.
(20) Bartók, A. P.; Kermode, J.; Bernstein, N.; Csányi, G. Machine Learning a General-Purpose Interatomic Potential for Silicon. *Phys. Rev. X* **2018**, *8*, 041048.
(21) Deringer, V. L.; Bernstein, N.; Csányi, G.; Ben Mahmoud, C.; Ceriotti, M.; Wilson, M.; Drabold, D. A.; Elliott, S. R. Origins of Structural and Electronic Transitions in Disordered Silicon. *Nature* **2021**, *589*, 59−64.
(22) Niu, H.; Bonati, L.; Piaggi, P. M.; Parrinello, M. Ab Initio Phase Diagram and Nucleation of Gallium. *Nat. Commun.* **2020**, *11*, 2654.
(23) Deringer, V. L.; Caro, M. A.; Csányi, G. A General-Purpose Machine-Learning Force Field for Bulk and Nanostructured Phosphorus. *Nat. Commun.* **2020**, *11*, 5461.
(24) Lin, B.; Jiang, J.; Zeng, X. C.; Li, L. Temperature-Pressure Phase Diagram of Confined Monolayer Water/Ice at First-Principles Accuracy with a Machine-Learning Force Field. *Nat. Commun.* **2023**, *14*, 4110.
(25) Piaggi, P. M.; Weis, J.; Panagiotopoulos, A. Z.; Debenedetti, P. G.; Car, R. Homogeneous Ice Nucleation in an Ab Initio Machine Learning Model of Water. *Proc. Natl. Acad. Sci. U.S.A.* **2022**, *119*, No. e2207294119.
(26) Blank, T. B.; Brown, S. D.; Calhoun, A. W.; Doren, D. J. Neural Network Models of Potential Energy Surfaces. *J. Chem. Phys.* **1995**, *103*, 4129−4137.
(27) Wörner, H. J.; Arrell, C. A.; Banerji, N.; Cannizzo, A.; Chergui, M.; Das, A. K.; Hamm, P.; Keller, U.; Kraus, P. M.; Liberatore, E.; Lopez-Tarifa, P.; Lucchini, M.; Meuwly, M.; Milne, C.; Moser, J.-E.; Rothlisberger, U.; Smolentsev, G.; Teuscher, J.; van Bokhoven, J. A.; Wenger, O. Charge Migration and Charge Transfer in Molecular Systems. *Struct. Dyn.* **2017**, *4*, 061508.
(28) Sharpless, C. M.; Blough, N. V. The Importance of Charge-Transfer Interactions in Determining Chromophoric Dissolved Organic Matter (CDOM) Optical and Photochemical Properties. *Env. Sci. Process. Impacts* **2014**, *16*, 654−671.
(29) French, R. H.; Parsegian, V. A.; Podgornik, R.; Rajter, R. F.; Jagota, A.; Luo, J.; Asthagiri, D.; Chaudhury, M. K.; Chiang, Y.; Granick, S.; Kalinin, S.; Kardar, M.; Kjellander, R.; Langreth, D. C.; Lewis, J.; Lustig, S.; Wesolowski, D.; Wettlaufer, J. S.; Ching, W.-Y.; Finnis, M.; Houlihan, F.; von Lilienfeld, O. A.; van Oss, C. J.; Zemb, T. Long Range Interactions in Nanoscale Science. *Rev. Mod. Phys.* **2010**, *82*, 1887−1944.
(30) Weck, P. F.; Balakrishnan, N. Importance of Long-Range Interactions in Chemical Reactions at Cold and Ultracold Temperatures. *Int. Rev. Phys. Chem.* **2006**, *25*, 283−311.
(31) Ringe, S. The Importance of a Charge Transfer Descriptor for Screening Potential CO_2 Reduction Electrocatalysts. *Nat. Commun.* **2023**, *14*, 2598.
(32) Rondi, A.; Rodriguez, Y.; Feurer, T.; Cannizzo, A. Solvation-Driven Charge Transfer and Localization in Metal Complexes. *Acc. Chem. Res.* **2015**, *48*, 1432−1440.
(33) Ojeda, J.; Arrell, C. A.; Longetti, L.; Chergui, M.; Helbing, J. Charge-Transfer and Impulsive Electronic-to-Vibrational Energy Conversion in Ferricyanide: Ultrafast Photoelectron and Transient Infrared Studies. *Phys. Chem. Chem. Phys.* **2017**, *19*, 17052−17062.
(34) Scarongella, M.; Laktionov, A.; Rothlisberger, U.; Banerji, N. Charge Transfer Relaxation in Donor-Acceptor Type Conjugated Materials. *J. Mater. Chem. C* **2013**, *1*, 2308−2319.
(35) Chen, X.-K.; Coropceanu, V.; Brédas, J. L. Assessing the Nature of the Charge-Transfer Electronic States in Organic Solar Cells. *Nat. Commun.* **2018**, *9*, 5295.
(36) Deng, Z.; Chen, C.; Li, X.-G.; Ong, S. P. An Electrostatic Spectral Neighbor Analysis Potential for Lithium Nitride. *npj Comput. Mater.* **2019**, *5*, 75.
(37) Artrith, N.; Morawietz, T.; Behler, J. High-Dimensional Neural-Network Potentials for Multicomponent Systems: Applications to Zinc Oxide. *Phys. Rev. B* **2011**, *83*, 153101.
(38) Morawietz, T.; Sharma, V.; Behler, J. A Neural Network Potential-Energy Surface for the Water Dimer Based on Environment-Dependent Atomic Energies and Charges. *J. Chem. Phys.* **2012**, *136*, 064103.
(39) Ko, T. W.; Finkler, J. A.; Goedecker, S.; Behler, J. A Fourth-Generation High-Dimensional Neural Network Potential with Accurate Electrostatics Including Non-Local Charge Transfer. *Nat. Commun.* **2021**, *12*, 398.
(40) Ko, T. W.; Finkler, J. A.; Goedecker, S.; Behler, J. Accurate Fourth-Generation Machine Learning Potentials by Electrostatic Embedding. *J. Chem. Theory Comput.* **2023**, *19*, 3567−3579.
(41) Jacobson, L. D.; Stevenson, J. M.; Ramezanghorbani, F.; Ghoreishi, D.; Leswing, K.; Harder, E. D.; Abel, R. Transferable Neural Network Potential Energy Surfaces for Closed-Shell Organic Molecules: Extension to Ions. *J. Chem. Theory Comput.* **2022**, *18*, 2354−2366.
(42) Zinovjev, K. Electrostatic Embedding of Machine Learning Potentials. *J. Chem. Theory Comput.* **2023**, *19*, 1888−1897.
(43) Unke, O. T.; Meuwly, M. PhysNet: A Neural Network for Predicting Energies, Forces, Dipole Moments, and Partial Charges. *J. Chem. Theory Comput.* **2019**, *15*, 3678−3693.
(44) Gao, A.; Remsing, R. C. Self-Consistent Determination of Long-Range Electrostatics in Neural Network Potentials. *Nat. Commun.* **2022**, *13*, 1572.
(45) Zhang, L.; Wang, H.; Muniz, M. C.; Panagiotopoulos, A. Z.; Car, R.; E, W. A Deep Potential Model with Long-Range Electrostatic Interactions. *J. Chem. Phys.* **2022**, *156*, 124107.
(46) Toukmaji, A. Y.; Board, J. A. Ewald Summation Techniques in Perspective: A Survey. *Comput. Phys. Commun.* **1996**, *95*, 73−92.
(47) Li, L.; Ciufo, R. A.; Lee, J.; Zhou, C.; Lin, B.; Cho, J.; Katyal, N.; Henkelman, G. Atom-Centered Machine-Learning Force Field Package. *Comput. Phys. Commun.* **2023**, *292*, 108883.
(48) Chanussot, L.; Das, A.; Goyal, S.; Lavril, T.; Shuaibi, M.; Riviere, M.; Tran, K.; Heras-Domingo, J.; Ho, C.; Hu, W.; Palizhati, A.; Sriram, A.; Wood, B.; Yoon, J.; Parikh, D.; Zitnick, C. L.; Ulissi, Z.

https://doi.org/10.1021/acs.jctc.3c01254
J. Chem. Theory Comput. 2024, 20, 2088−2097

Open Catalyst 2020 (OC20) Dataset and Community Challenges. *ACS Catal.* **2021**, *11*, 6059−6072.
(49) Kresse, G.; Hafner, J. Ab Initio Molecular-Dynamics Simulation of the Liquid-Metal-Amorphous-Semiconductor Transition in Germanium. *Phys. Rev. B* **1994**, *49*, 14251−14269.
(50) Novikov, I. S.; Shapeev, A. V. Improving Accuracy of Interatomic Potentials: More Physics or More Data? A Case Study of Silica. *Mater. Today Commun.* **2019**, *18*, 74−80.
(51) Henkelman, G.; Arnaldsson, A.; Jónsson, H. A Fast and Robust Algorithm for Bader Decomposition of Charge Density. *Comput. Mater. Sci.* **2006**, *36*, 354−360.

https://doi.org/10.1021/acs.jctc.3c01254
J. Chem. Theory Comput. 2024, 20, 2088−2097